A forward reconstruction, holographic method to overcome the lens effect during 3D detection of semitransparent, non-spherical particles

Cheng-Wei Tai,[a] Adib Ahmadzadegan,[b], Arezoo Ardekani,[*b] and Vivek Narsimhan[*a]

Suspension of semi-transparent particles such as polystyrene microparticles are commonly used as model systems in the study of micro-rheology, biology and microfluidics[1–3]. The ability of resolve individual particle position and orientation can provide better understanding of the these dynamic systems. When one examines holograms of semi-transparent spheroids with an $O(1)$ aspect ratio, the lens effect from the particle introduces complex patterns that makes it difficult to analyze the particle position and orientation. We propose a reconstruction method that uses image moment information to generate a mask over the sharp patterns from the lens effect and gives reasonable estimation of the 3-D position and orientation of the particle. The method proposed in this work uses the average particle geometry information to determine the process parameters and identify the proper detection zone. The average detection error for z_c is less than 25% of the average particle thickness, and the average errors in the in-plane and out-of-plane orientations ϕ and θ are 2° and 4°, respectively. Our method provides comparable accuracy in the detection of particle center of mass (x_c, y_c, z_c) and in-plane orientation ϕ as a recent forward reconstruction method for semi-transparent particles proposed by Byeon et al.[4,5]. This method provides a clearly defined framework for identifying the particle's out-of-plane tilt angle θ . We finally demonstrate the applicability of the method to opaque, slender (aspect ratio $A_R \gg 1$) particles by analyzing the 3-D motion of an E. coli cell from holographic video footage.

1 Introduction

The ability to resolve the three-dimensional (3-D) position and orientation of a dynamic, orientable particle is crucial to analyze systems seen in various fields such as biology, rheology, oceanography and industrial safety[6–9]. Specifically in microbiology, the collective motion of microswimmers such as bacteria cells near phase boundaries governs the formation of biofilms, which is crucial in the field of microbial pathology and ecology[10–13]. In microrheology, the 3-D translational and rotational motion of a non-spherical particle can be used to probe the rheological properties of the suspending fluid[2,14–16]. The ability to track the 3-D particle motion is also important in industrial applications such as dust explosion and combustion safety[9,17].

For a suspension of particles with a characteristic time scale of variation less than $O(1)$ seconds, tracking the 3-D motion of these particles using typical imaging methods is in general not straightforward. Typical imaging methods such as bright-field and confocal microscopy require a layer-by-layer volume scan during the experiment time. This process typically requires minutes to complete, which results in a limited temporal resolution for fast-changing systems with a shorter time scale of variation[18–20].

One possible way to resolve this problem is to adopt imaging methods based on holographic imaging techniques. Digital holographic microscopy (DHM) utilizes a coherent light source (laser) to illuminate the target object. The incident light wave in combination with the scattered light wave from the target object gives a 2-D image known as a hologram[21–24]. A hologram contains the 3-D information such as the position and orientation of the target object. These holograms can be stored for offline numerical reconstruction. This property eliminates the need for a full-volume scan during the experimental time, which makes DHM specifically suitable for studying a fast-changing system. The temporal resolution of DHM is only determined by the camera speed. DHM is also more suitable for a dilute suspension system to maintain a clean diffraction pattern for numerical reconstruction[23,24].

Reconstructing the 3-D position and orientation of a non-spherical particle from a hologram can be challenging. For a spherical particle, the exact solution to the scattering patterns

---

[a] *Davidson School of Chemical Engineering, Purdue University, 480 W Stadium Ave, West Lafayette, IN 47907, USA;*

[b] *School of Mechanical Engineering, Purdue University, 585 Purdue Mall, West Lafayette, IN 47907, USA*

[*] *E-mail: ardekani@purdue.edu, vnarsim@purdue.edu*

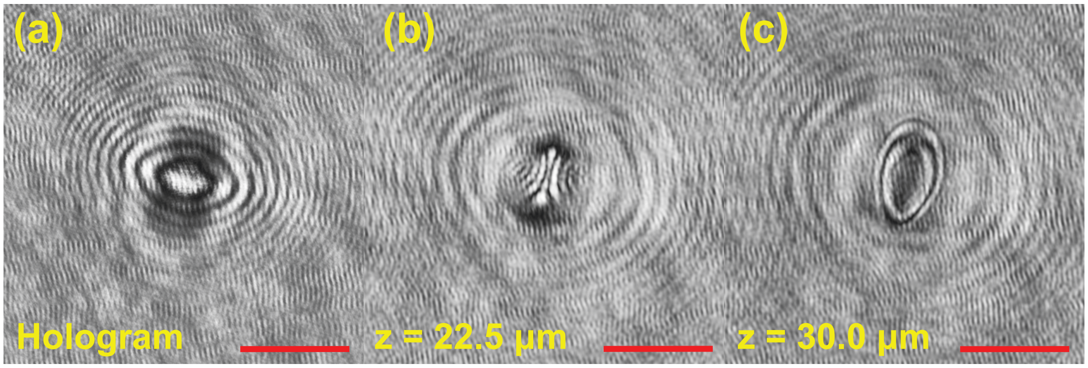

Fig. 1 (a) The hologram of a semi-transparent, prolate-shaped polystyrene particle taken at 30 μm below the particle center of mass. (b) Due to the lens effect induced by particle transparency, light beams cross at z positions off from the particle center of mass and generate sharp diffraction patterns. (c) The reconstructed hologram at the particle center of mass. The sharp patterns mark the particle contour. The scale bar is 10 μm. We enhanced the image contrast for better visibility of the hologram patterns.

is available through the well-known Lorentz-Mie scattering theory[25,26]. One can easily retrieve the particle position by fitting the scattering patterns from the hologram to the solution[27,28]. On the contrary, reconstructing the position and orientation of a non-spherical particle is generally difficult due to their orientability. A non-spherical particle can generate distinct scattering patterns at different orientations which largely complicates the reconstruction process. There are two major pathways to reconstruct the 3-D information of a non-spherical particle. One class of the methods solve the reverse problem by simulating a library of holograms at different orientations and retrieve a best-fit solution to the experimental hologram using rigorous statistical inference algorithms[28–31]. This type of generative method can resolve down to wavelength-sized particles, yet the simulation and inference process can be time consuming and computationally intensive[4,5,31].

The other class of methods solves the forward problem by utilizing the information contained in the experimental holograms to reconstruct the position and orientation of the particle. A hologram is first numerically propagated along the optical axis direction to retrieve images at different depth positions. From this stack of images, one can then determine the center of mass and the orientation of the target object using additional image processing methods[7,19,22,23,32]. This implementation is relatively straightforward and we will focus our discussion on such type of methods.

The reconstruction process for the 3-D position and orientation of an object largely depends on its geometry and material properties. For a stringy object such as a fiber and malaria cells, one can reconstruct their position and orientation by fitting the object skeleton to line segments[33–36]. For an opaque object that reflects or absorbs light, one can apply commonly used focusing functions (e.g. variance of the gradient profile or Laplacian of the image profile)[37,38] to evaluate the image sharpness and determine the position of the object in the 3-D space[7,9,32]. For semi-transparent objects with $O(1)$ aspect ratio (e.g. polystyrene particles in PDMS gel, biological cells in aqueous medium, oil-water emulsions), the reconstruction methods used for opaque, needle-like particles could fail due to the more ambiguous particle boundaries and complex diffraction patterns introduced by lens effect[4,5]. Figure 1 shows an example of reconstructed image series from a hologram generated by a semi-transparent, ellipsoidal polystyrene particle located at 30μm above the hologram plane (figure 1a). Aside from the sharp boundary seen in the in-focus image (figure 1c), one can also observe sharp diffraction patterns due to the particle transparency at other out-of-focus locations (figure 1b).

These sharp patterns can give strong response to the focusing functions and lead to incorrect detection results if one tries to determine the object's position by the strongest response from the focusing function. An alternative reconstruction method is thus necessary to handle these type of semi-transparent particles.

In this manuscript we will focus our discussion on semi-transparent ellipsoidal particles which is the simplest type of non-spherical particle. One available method proposed by Byeon et al.[4],[5], Seo et al.[39] treats the particle as a convex lens. Once the location of the focal point is known (e.g., where the light beam crosses after passing through the lens, figure 1b), one can calculate the focal length of the lens to determine particle position in the optical axis direction. The in-plane orientation ϕ can be determined by using simple thresholding to reveal orientation of the bright stripe formed at the focal point. To determine the out-of-plane tilt angle, the method extracts pixels along the particle major axis at different z layers. A thresholding is applied to the resulting image to visualize how the focal pattern is tilted in the depth direction. The out-of-plane tilt angle is determined by the angle between the hologram plane and the line formed by connecting the thresholded focal pattern at the two ends of the particle[4,5]. The method shows good accuracy in measuring particle position and orientations. However, the detection scheme for the out-of-plane tilt angle relies on an ambiguously defined procedure and the results may be sensitive to the threshold criteria applied to extract the diffraction feature[5].

The main goal of this work is to provide a straightforward and clearly defined method to reconstruct the 3D position and orientation of an orientable particle. We propagate the holograms using angular spectrum method and determine the particle posi-

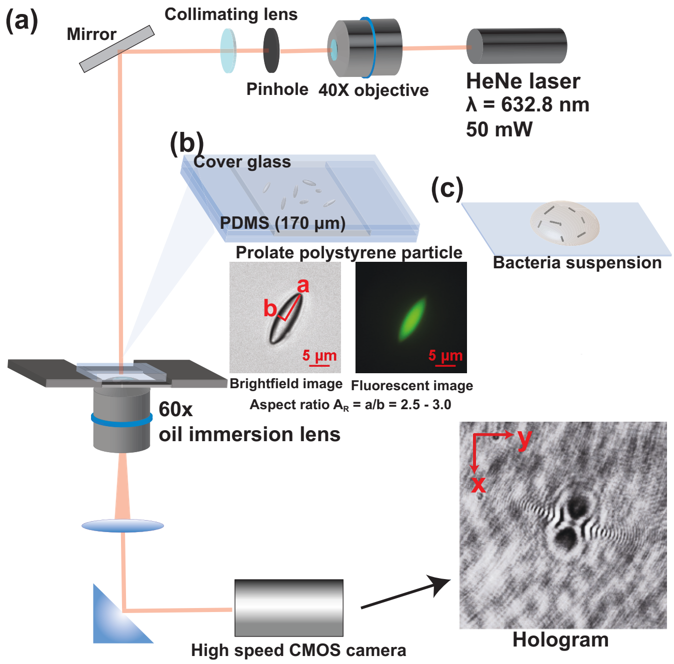

Fig. 2 (a) Holography experimental setup. We use a Helium-Neon laser (λ = 632.8 nm) with 50 mW power as the light source. The holograms are visualized under an inverted microscope with a 60x oil immersion lens and captured using a CMOS high speed camera. (b) The fluorescent, prolate PS particles are embedded in a PDMS gel inside a 170 μm thick glass chamber. (c) For visualizing E. coli cell sample, we place 500 μL of the suspension as prepared in section 2.2 on a microscopy cover slip and follow the same imaging procedure to retrieve the video footage of the cell motion. We enhanced the hologram contrast for better visibility of the diffraction patterns.

tion in the depth direction by quantifying the image sharpness in these propagated images. We then extract the location of the particle boundary and determine the particle's in-plane and out-of-plane orientation. For semi-transparent particles, we use the image moment information to generate a mask that covers the sharp diffraction pattern from the lens effect. This allows us to better resolve the location of the particle contour. This work provides a better-defined and straightforward framework to reconstruct the 3-D information of a non-spherical particles. The method requires the knowledge of the average particle dimension to determine the process parameters. This method gives similar accuracy in detecting the particle center of mass and in-plane orientation as a recent method by Byeon *et al.* (2016) for semi-transparent ellipsoids[4,5]. We also demonstrate the applicability of our method on analyzing the motion of slender, opaque E. coli cells.

The paper is arranged as follows: section 2 introduces the materials and setup for the holography experiments. Section 3 details the hologram reconstruction procedure for determining the particle center of mass and orientation using image moment information. Section 4 shows results. We will first measure the position and orientation of fluorescent, semi-transparent ellipsoidal polystyrene particles embedded in PDMS gel, and compare the results to grouth-truth measurements from confocal microscopy experiments. We will then demonstrate the ability of the method to resolve the motion of E. coli cells in an aqueous medium. Section 5 concludes this work.

2 Experimental setup

2.1 Fabrication of stagnant prolate polystyrene microparticle sample in PDMS gel

We adapt the methodology by Ho et al.[40], Champion et al.[41] for fabricating non-spherical polystyrene microparticles. Fluorescent polystyrene particles (PS, average diameter 6 μm, coefficient of variation 10%, $n_{PS} = 1.59$, Fluoresbrite®YG, Polysciences, Inc.) are dispersed in an aqueous solution of polyvinyl alcohol (PVA, 5 $wt.\%$, $M_w = 84 - 125 kDa$, Sigma-Aldrich) and Glycerin (2.5 $wt.\%$, Fisher Scientific). The suspension is cast into a flat stainless steel plate (Cole-Parmer) and dried under room temperature for 24 hours to form a stretchable film with average thickness of 140 μm. The film is trimmed to the desired size and loaded onto a custom-made stretching device. The loaded device is submerged in a silicone oil bath at 130$^{\circ}C$ and stretched to the desired amount. The film sections that contain desired particle geometry are cut washed with hexane (Fisher Scientific) and dissolved in water to remove PVA. The particles are triple-washed with water then recovered by centrifugation. We collect particles that has aspect ratio A_R in the range of 2.5 to 3.0.

The stretched particles are dried under vacuum for 2 hours. The dried PS particles are then re-suspended in hexane (Fisher Scientific) and mixed with polydimethylsiloxane elastomer base (PDMS, Sylgard 184, $n_{PDMS} = 1.42$ at 632.8 nm, Dow-Corning). The hexane is removed under vacuum and the curing agent is added into the elastomer mixture after the removal of hexane. The mixture is then degassed under vacuum and sealed in a chamber of 170 μm in thickness made with cover glasses (Thermofisher Scientific) figure 2. The PDMS mixture is then cured at 80$^{\circ}C$ for 4 hours.

2.2 Preperation of E. coli sample

Motile Escherichia coli (HCB-437) was cultured as described in Ahmadzadegan *et al.* (2019)[42] and re-suspended in a motility medium (10^{-2} M potassium phosphate, pH 7.0, 10^{-4} M EDTA). A 500 μL of the solution is then placed on microscopy cover glass and imaged.

2.3 In-line holographic microscopy setup

The digital inline holography setup was modified from the setup described in Molaei *et al.* (2014)[43]. We used a HeNe Laser with a wavelength of 632.8 nm (Melles Griot). A 60X Nikon objective lens focuses the laser beam onto a 50 μm pinhole (Thorlabs) and a convex lens with a 50 mm focal length is placed at the distance of 50 mm from the pinhole to create a collimated beam of light that is directed towards the sample on a microscope.

2.4 Confocal microscopy setup

A spinning disk confocal module (Crest Optics) is attached to a Nikon Ti microscope to simultaneously capture images from both the holography setup as well as benchmark the location and orientation from a confocal z-slice scan.

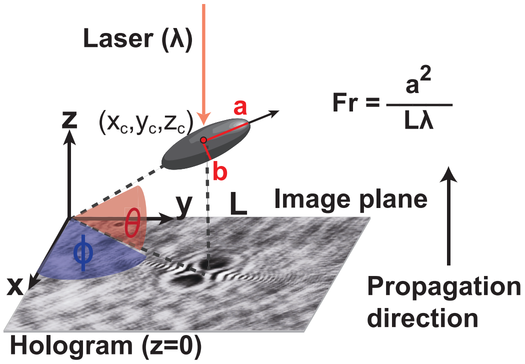

Fig. 3 Schematic of coordinate system. The image plane is in the $x-y$ plane and the optical axis is along the $z-$axis. The wavelength of the laser is λ. The hologram plane is defined to be in the plane of $z=0$. The particle's center of mass is at (x_c,y_c,z_c) and the semi-major and minor axes lengths are a and b, respectively. The particle aspect ratio is $A_R=a/b$. The particle orientation is defined based on the particle's axis of symmetry. The azimuth angle ϕ is the angle between the positive $x-$axis and the projection of the particle's axis of symmetry on the $x-y$ plane. The altitude angle θ is the angle between the particle's axis of symmetry and the $x-y$ plane. The holograms are propagated in the positive z direction. We use Fresnel number $Fr=a^2/L\lambda$ to characterize the optical regime. We enhanced the hologram contrast for better visibility of the diffraction patterns.

3 Hologram reconstruction and particle position/orientation detection

The system and coordinate definition is summarized in figure 3. Here we adopt a dimensionless group Fresnel number Fr to characterize the optical regime:

$$Fr=\frac{a^2}{L\lambda}, \tag{1}$$

where a is the characteristic size of the object, λ the wavelength of the illumination beam, and L the observation distance from the particle center of mass. Here we choose the semi-major axis length of the particle the characteristic size. In general, $Fr\geq 1$ denotes the near field regime and $Fr<1$ represents the far field regime.

The captured holograms are first processed with background subtraction to improve the image quality. The processed hologram is then numerically propagated along the optical axis direction using angular spectrum method to retrieve images at different depth positions[22]. We then apply image moment techniques to detect the particle center of mass and orientation. We will introduce the image processing steps in the following sections.

3.1 Hologram propagation

The hologram $U(x,y;z=0)$ is numerically propagated along the optical axis direction to retrieve the image at different z positions (figure 4c). The propagated image $U(x,y;z=z_i)$ at plane $z=z_i$ is calculated by the following equation[22]:

$$U(x,y;z=z_i)=\mathscr{F}^{-1}\left\{\mathscr{F}[U(x,y;z=0)]\exp\left[-i2\pi z_i\sqrt{\frac{1}{\lambda^2}-f_x^2-f_y^2}\right]\right\}, \tag{2}$$

where f_x,f_y represents the spatial frequency in the x,y direction respectively in the frequency space, λ the laser wavelength, and $\mathscr{F},\mathscr{F}^{-1}$ the forward and inverse 2D fast Fourier transform (2D-FFT/2D-iFFT), respectively. The angular spectrum method models the propagation of light waves as a superposition of infinite number of planar waves. The method is in general valid in the near-field regime $(Fr\geq 1)$[22].

3.2 Particle center of mass and orientation detection

3.2.1 Center of mass detection

For an image $I(x,y)$, we define the a-th moment in the x direction and b-th moment in the y direction m_{ab} by the following equation:

$$m_{ab}(I(x,y))=\sum_{i=1}^{N_x}\sum_{j=1}^{N_y}x_i^a\,y_j^b\,I(i,j), \tag{3}$$

where N_x, N_y represents the number of pixels of the image in the x and y direction, respectively.

To determine the center of mass in the $x-y$ plane, we apply thresholding to the processed hologram $U(x,y;z=0)$ (eqn. (4)) to get the thresholded image $T(x,y;z=0)$. For the pixels in $U(x,y;z=0)$ that meet the threshold criteria C_{th}, we assign the corresponding pixel value in $T(x,y;z=0)$ to be 1 (positive pixels) and others to be 0 (negative pixels). We then estimate the in-plane center of mass x_c,y_c by averaging the x and y position of the positive pixels in thresholded image via eqn. (5) (figure 4b)[44,45]:

$$T(x,y;z=0)=\begin{cases}1 & \text{if } U(x,y;z=0)\in C_{th}\\ 0 & \text{if } U(x,y;z=0)\notin C_{th}\end{cases} \tag{4}$$

$$(x_c,y_c)=\left(\frac{m_{10}}{m_{00}},\frac{m_{01}}{m_{00}}\right). \tag{5}$$

We next determine the out-of-plane canter of mass z_c of the particle by image sharpness. In each propagated image $U(x,y;z=z_i)$, we examine a window around (x_c,y_c) of width W_c (i.e. $|x-x_c|\leq W_c/2,|y-y_c|\leq W_c/2$) that covers the entire particle. For the $A_R=3$ prolate particles used in this work, we set $W_c=2.5a\approx 15\mu m$, or 2.5 times of the average particle semi-major axis length to ensure the coverage of the target particle. At each z_i, we convolve the Sobel filter on the center window image in both the x and y directions to calculate the horizontal and vertical image gradient profiles G_{x,z_i},G_{y,z_i} of the image at each propagation layer (eqn.

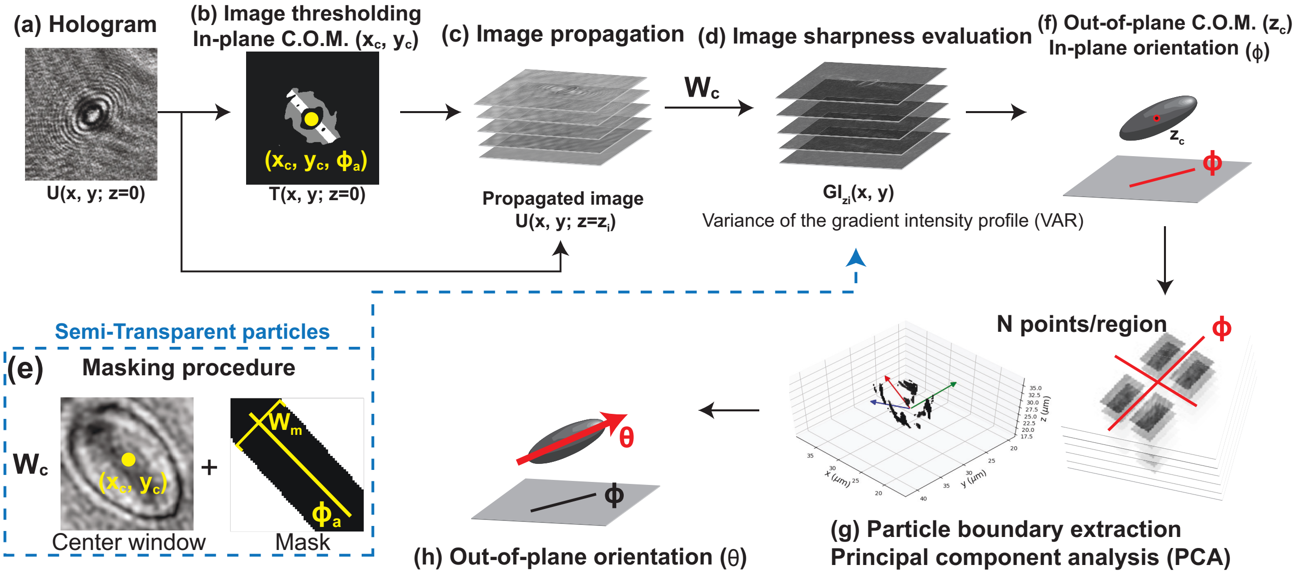

Fig. 4 Reconstruction flow chart for identifying particle center of mass (x_c, y_c, z_c) and orientation (ϕ, θ). (a) Original hologram. (b) The hologram is thresholded to determine the in-plane center of mass (x_c, y_c) and the approximate in-plane angle ϕ_a. (c) The original hologram is numerically propagated to reconstruct images at different z positions. (d) For each z layer, the image sharpness is evaluated in a box of width W_c centered around (x_c, y_c). This procedure allows one to identify the out-of-plane center of mass z_c. (e) For semi-transparent particles, a mask of width W_m along the particle's major axis is added to the sharpness evaluation step to improve the detection accuracy for z_c. (f) The in-plane orientation angle ϕ is determined by calculating the image moments of the superimposed gradient intensity profile around z_c. (g-h) We finally extract the particle boundary and perform PCA to determine the out-of-plane tilt angle θ. We enhanced the hologram contrast in this figure for better visibility of the diffraction patterns.

(6)-(7))[7,32].

$$Sb_x = \begin{bmatrix} 1 & 0 & -1 \\ 2 & 0 & -2 \\ 1 & 0 & -1 \end{bmatrix}, \quad Sb_y = Sb_x^T \tag{6}$$

$$G_{x,z_i} = U(x,y;z=z_i) * Sb_x,\ G_{y,z_i} = U(x,y;z=z_i) * Sb_y$$

$$\text{for } |x - x_c| \le W_c/2,\ |y - y_c| \le W_c/2, \tag{7}$$

where $*$ represents a 2-D convolution operation. We next define the gradient intensity profile $GI_{z_i}(x,y)$ at $z = z_i$ to be the l_2 norm of the horizontal and vertical gradient profile at the corresponding position (eqn. 8). For each layer $z = z_i$, we calculate the variance of the gradient intensity profile (VAR) as a metric for the image contrast and sharpness[37,46].

$$GI_{z_i}(x,y) = \sqrt{G^2_{x,z_i}(x,y) + G^2_{y,z_i}(x,y)} \tag{8}$$

$$VAR_{z_i} = \sum_{i=1}^{Wc}\sum_{j=1}^{Wc}\left[GI_{z_i}(i,j) - \mu_{z_i}\right]^2, \quad \mu_{z_i} = \frac{1}{W_c^2}\sum_{i=1}^{Wc}\sum_{j=1}^{Wc} GI_{z_i}(i,j) \tag{9}$$

where μ_{z_i} and VAR_{z_i} are the mean value and the variance of the gradient intensity profile at $z = z_i$, respectively. A sharp pattern (abrupt change in pixel value) will generate strong gradient values in the nearby pixels in the gradient profile and lead to a high variance value. For an optically opaque particle (e.g. coal particle, metallic nano-particles), sharp patterns appear only when the target object is in focus[27,32]. We can therefore pick the z layer that gives the highest variance value to be the particle center of mass in the z direction, or $z_c = \text{argmax}(VAR_{z_i})$. For a semi-transparent particle (e.g. ellipsoidal polystyrene particle), however, the particle can act as a lens and generate sharp patterns at z positions near the focal point of the lens[4,5]. For such type of particle, we often observe a wide peak in the image gradient variance profile along the z direction that spans from the focal point to the particle center of mass. The black curve in figure 5a shows the VAR intensity with respect to z position for a semi-transparent prolate polystyrene particle. In this case, the diffraction patterns that appear around the focal point (figure 5b) can also give a strong response in VAR. Picking the z that gives the strongest VAR response may not guarantee the correct z_c position of the particle. To handle this issue, we additionally impose a mask during the image variance calculation process to help us better identify the location of the particle center of mass.

For the original hologram $U(x,y;z=0)$, we apply thresholding and eqn. (11) (described in next subsection) to calculate the approximated in-plane orientation ϕ_a of the particle. A mask along the direction of ϕ_a with width W_m is applied to the center window $|x - x_c| \le W_c/2, |y - y_c| \le W_c/2$ during the image sharpness evaluation step (figure 4d, 5c). The mask covers the center region of the particle and the diffraction patterns appearing within the mask is neglected during the image sharpness evaluation step. The red line in figure 5a shows the VAR profile along z direction after applying a mask with $W_m = 1.6b$. The application of the mask divides the bulk peak into two major regimes. The first regime covers the z layers that contain the diffraction patterns seen before the particle comes into focus, and the second peak appears at the z layer that the particle is in focus (figure 5b)[4,5,32]. We will then pick z location of the second major peak as the location of the particle

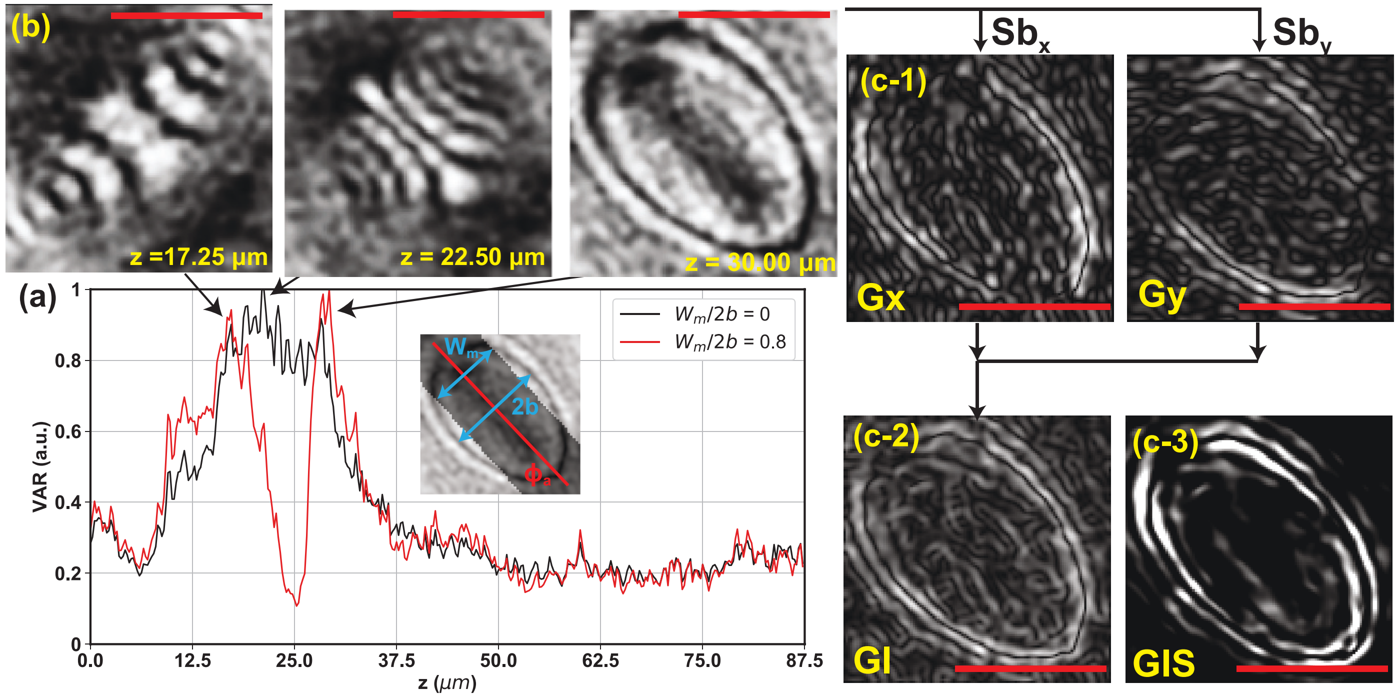

Fig. 5 (a) Variance of the gradient intensity profile VAR at different z layers from one of the sample particles. The center of mass of the particle is identified to be $z_c = 30.00\mu m$ based on confocal measurements. The black and red lines represent the profile with and without the center mask, respectively. The inset illustrates the center mask. The mask covers the pixels along the particle's major axis direction with width W_m. The gradient intensity values inside the mask are neglected when calculating VAR. In the plot, the variance profiles are normalized by the max variance of the individual profiles. The center box width for calculating VAR is $W_c = 2.5a$. (b) Reconstructed images of the propagated holograms at different z locations. (c-1) The horizontal and vertical gradient profiles G_x and G_y at $z = 30.00\,\mu m$. (c-2) Total gradient intensity profile (GI), which is the l_2 norm of G_x and G_y (eqn. 8). The variance of GI (VAR) is used as the metric to quantify image sharpness and hence identify z_c. (c-3) The superimposed gradient intensity profiles GIS in $|z - z_c| \leq 2.5\,\mu m$. The scale bar is $5\,\mu m$. We enhanced the hologram contrast in this figure for better visibility of the diffraction patterns. For figure (b) and (c), no mask is applied to better visualize the lens effect pattern or particle contour.

z center of mass for such type of semi-transparent particles. The rule of thumb for picking the width of the center mask is that W_m should be less than twice the the particle minor axis length, or $W_m < 2b$. For this work, we will use mask with width that is 80% of of this criterion, or $W_m = 1.6b$.

3.2.2 Orientation detection

For the in-plane orientation angle ϕ, we sum up the gradient intensity profiles in $|z - z_c| \leq 2.5\,\mu m$ to get the superimposed gradient intensity profile GIS (equation 10, figure 5d-3). We then apply eqn. (11) to the threshold image of GIS profile to determine the in-plane orientation of the particle[44,45].

$$GIS = \sum_z GI_z(x,y), \ \text{for} |z - z_c| \leq 2.5\mu m, \tag{10}$$

$$\phi = \frac{1}{2}\tan^{-1}\left[\frac{2(\frac{m_{11}}{m_{00}} - x_c y_c)}{(\frac{m_{20}}{m_{00}} - x_c^2) - (\frac{m_{02}}{m_{00}} - y_c^2)}\right] \tag{11}$$

For detecting the out-of-plane angle θ, we extract the gradient intensity profiles between $|z - z_c| \leq a$, where a is the semi-major axis length of the particle. We divide the profile into 4 regions based on the detected direction of the particle major and minor axis (figure 4f). For each region, we record the coordinates of the first N strongest gradient intensity pixels within the region over $|z - z_c| \leq a$. We then combine the data for all four regions and calculate the covariance matrix of the coordinate data to characterize their distribution in the 3-D space. This process is known as principal component analysis (PCA). From the covariance matrix we extract the eigenvector $\mathbf{E} = (E_x, E_y, E_z)$ with the highest eigenvalue and use eqn. (12) to determine the out-of-plane orientation θ:

$$\theta = \tan^{-1}\left(\frac{E_z}{\sqrt{E_x^2 + E_y^2}}\right). \tag{12}$$

4 Results

In section 4.1-4.4, we perform tests to study the effect of different process parameters on the reconstruction results, and verify the accuracy of the proposed methodology. For these tests we use stagnant, fluorescent polystyrene particles prepared in section 2.1 as our model particles. We embed these particles in a PDMS gel and randomly select 12 particles from the sample and record their holograms at $L = 30$, 40, 50 and 75 μm from the particle center of mass. For an $A_R = 3$ prolate particle with $a = 6.24\,\mu m$, the Fresnel number is 2.05, 1.54, 1.23, 0.82, respectively. We compare the holography results to measurements from confocal microscopy, which we regard as the "ground truth". In section 4.5, we illustrate how standard line fitting methods in the holography literature do not accurately capture particle orientation for semi-transparent particles with $O(1)$ aspect ratio. This phenomnenon

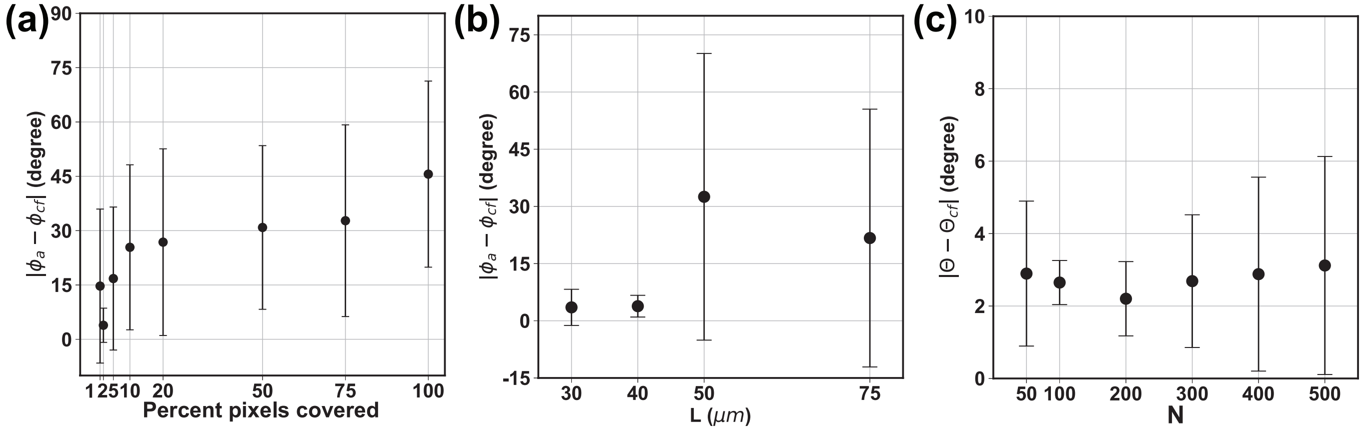

Fig. 6 (a) The average absolute detection error between the approximate and confocal detected in-plane angle $|\phi_a - \phi_{cf}|$ for the 12 sample particles using different thresholding criteria for the lowest intensity pixels. (b) The average absolute error between the approximate and confocal detected in-plane angle $|\phi_a - \phi_{cf}|$ for the 12 sample particles at various observation distances $L = 30, 40, 50, 75 \mu m$. We use C_{th} that covers the first 2-5 % lowest intensity pixels for thresholding. (c) The average absolute detection error between the holography and confocal detected out-of-plane angle $|\theta$ - $\theta_{cf}|$ for the 12 sample particles using various number of points N in the principal component analysis. The holograms used in this test are taken at $L = 30\mu m$. The process parameters for these tests are $W_c = 2.5a$ and $W_m = 1.6b$. The error bars in these plots represent 1 standard deviation of the angle error for the 12 model particles.

arises from the lens effect, and the masking procedure introduced in this paper allows one to overcome this issue to correctly identify particle orientation. Lastly, in section 4.6 we demonstrate the ability of this method to analyze the 3-D motion of E. coli cells in an aqueous medium from holographic video footage.

4.1 Effect of thresholding criteria C_{th} on mask generation

A proper choice of thresholding criteria can provide us a good estimation of the in-plane orientation ϕ_a and thus generate a mask that can help us more precisely locate the particle boundary. For the 12 sample particles, we use the holograms taken at $L = 30\,\mu m$ for the test. For each raw hologram, we apply different threshold values C_{th} and use the pixels with values lower than C_{th} to calculate the approximate in-plane angle ϕ_a. Fig 6 reports the average absolute difference between the approximate and confocal experiment captured in-plane angle $|\phi_a - \phi_{cf}|$ versus the percentage of total number of pixels used for ϕ_a calculation. We see the error is minimum for the in-plane when the threshold value covers the first 2 to 3 % of lowest intensity pixels. The error becomes significant when too few or many pixels are used in the calculation. The detected ϕ_a approaches 45° when all the pixels are used in the calculation. We therefore choose C_{th} that covers no more than the first 2-5% lowest intensity pixels for ϕ_a calculation and mask generation. Here we take the 2nd to 5th percentile pixel value from the histogram of the hologram as the threshold value.

4.2 Effect of observation distance on mask generation

We next discuss how the observation distance L affects detection of approximate in-plane angle ϕ_a as well as the mask generation results. For semi-transparent particles, the generation of a mask relies on a good approximation of the particle in-plane angle from the raw hologram. For the 12 sample particles we use holograms taken at $L = 30, 40, 50, 75\mu m$ and use C_{th} that extracts the first 2-5% lowest intensity pixels for thresholding. We compare the resulting ϕ_a to the confocal experiment measurement ϕ_{cf} to quantify the quality of the detection. We report the average absolute angle difference $|\phi_a - \phi_{cf}|$ for the 12 sample particles at different observation distance L in figure 6b. We see that for the aspect ratio 3 prolate particle used in the test, the average error is about 4 degrees at $L = 30, 40\mu m$. As we move farther away from the particle towards the far-field regime, the diffraction pattern in the raw hologram spreads wider along the minor axis direction and the estimated in-plane angle ϕ_a deviates farther from the correct major axis direction. At a far enough observation distance from the particle center of mass (e.g. $L = 75\,\mu m$ in figure 7a), our procedure incorrectly captures the minor axis direction of the particle as ϕ_a, which introduces a 90 degree error from the particle major axis. For the 12 sample particles used in this test, we see this phenomenon for 4 particles at $z = 50\,\mu m$ and 2 particles at $z = 75\,\mu m$.

4.3 Effect of PCA parameter N on detection results

We next discuss how the number of points used in the principal component analysis affects the detection of the out-of-plane angle θ angle (figure 4f). For the 12 sample particles, we use the holograms taken at $L = 30$ μm and measure their θ angle using N =50, 100, 200, 300, 400, 500 for each of the four regions (200, 400, 800, 1200, 1600, 2000 total number of pixels, respectively). The reconstructed θ are compared to the confocal reconstruction θ_{cf} to calculate the reconstruction error. The plot of the average absolute error $|\theta - \theta_{cf}|$ with respect to N for the 12 sample particles is shown in figure 6c. We see that the averaged absolute error in θ angle for different N is within 3 degrees, with $N = 200$ giving the smallest average error. When an inadequate number of pixels ($N < 200$) is used in the analysis, the pixels cannot properly capture the contour of the particle, and therefore gives a larger deviation from the correct value. On the other hand, as more

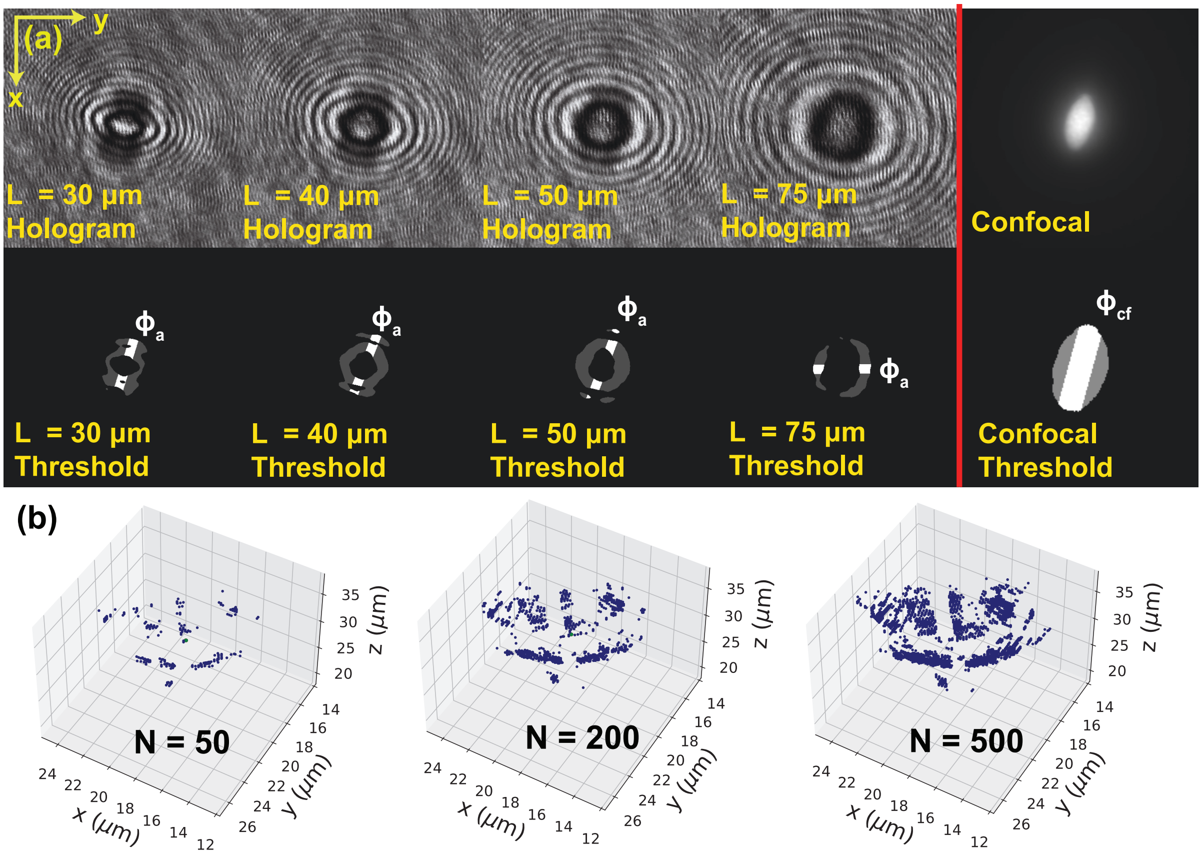

Fig. 7 (a) Holograms and thresholded images of a sample particle taken at $L = 30, 40, 50, 75 \mu m$ from the particle center of mass. The confocal image of the particle is shown on the right for comparison. We use C_{th} that covers 2 to 5 % lowest intensity pixels for thresholding. We calculate the approximate in-plane angle ϕ_a using equation 11 and compare against the "ground-truth" value ϕ_{cf} from the confocal image. All angles are visualized as white lines in the thresholded images. We enhanced the hologram contrast for better visibility of the patterns. (b) The image of the extracted particle contour from principal component analysis using $N = 50, 200, 500$. The particle center of mass is located at $z_c = 30\,\mu m$.

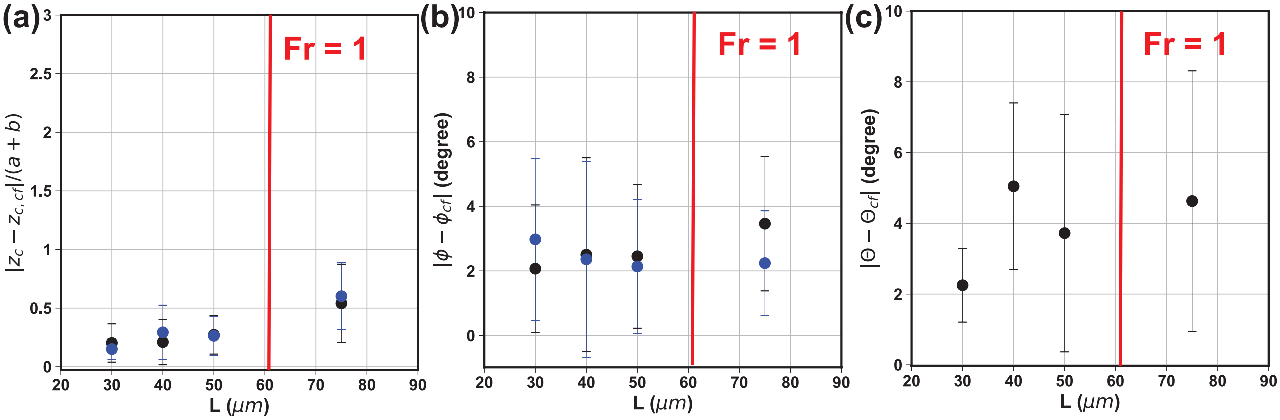

Fig. 8 Plots of the (a) normalized, absolute average error of z_c, (b) absolute average error of ϕ angle, (c) absolute average error of θ angle with respect to the observation distance L from the particle center of mass for the 12 sample particles. The error is calculated by the difference between the confocal reconstruction $(z_{c,cf}, \phi_{cf}, \theta_{cf})$ and holographic reconstruction (z_c, ϕ, θ). The error bar represents one standard deviation of the error from the 12 sample particles at each L. The reconstruction error using the method proposed by Byeon *et al.* (2016)a, b[4,5] is shown in blue color for comparison. The vertical red line located at $L =$ 61.5 μm marks the location where $Fr = 1$ using $a = 6.24\,\mu m$, $\lambda = 0.6328 \mu m$. The error in z_c is normalized by the average particle size $(a + b)$.

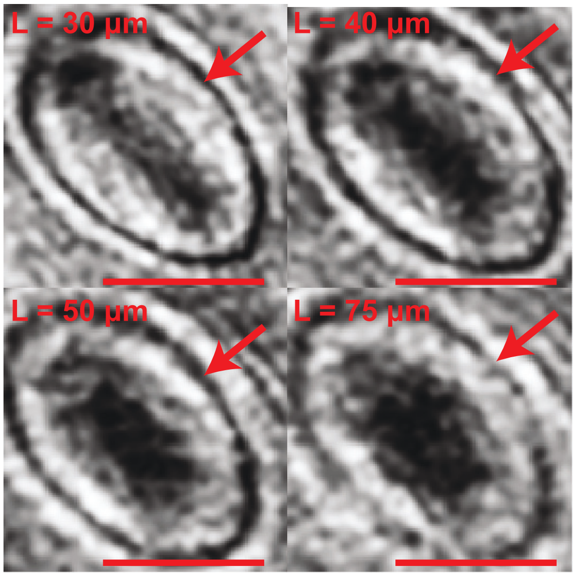

Fig. 9 The reconstructed image at $z = z_c$ for an identical, semi-transparent polystyrene particle from various observation distances $L = 30, 40, 50, 75\,\mu m$ with Fr =2.05, 1.54, 1.23, 0.82, respectively. The reconstructed image shows a less well-defined particle boundary (red arrow) as the observation distance L increases. This is due to the attenuation of light through a thicker layer of PDMS gel as well as the limitation of the angular spectrum method. The scale bar is 5 μm. We enhanced the image contrast for better visibility of the particle contour.

pixels ($N > 200$) are used in the PCA, the data set can contain excessive noise in addition to the particle contour location, and the PCA tends to give incorrect detection results. Figure 7b shows an example of the extracted particle contour using different number of points. We thus choose $N = 200$ for the PS prolate particles used in this work.

4.4 Reconstruction results verification

We use the same set of 12 particles to verify the reconstruction accuracy of our method. The captured holograms are reconstructed using the proposed method to retrieve the particle's position and orientation $(x_c, y_c, z_c, \phi, \theta)$. The results are compared to the confocal reconstruction results $(x_{c,cf}, y_{c,cf}, z_{c,cf}, \phi_{cf}, \theta_{cf})$ to calculate the error. We specifically report the results for z_c, ϕ and θ. Here we pick the process parameters to be the following: threshold value C_{th} = 3rd percentile pixel intensity, center window width $W_c = 2.5a$, center mask width $W_m = 1.6b$ and the number of points used in principal component analysis in each section $N = 200$. Figure 8a shows the error in z_c normalized by the average particle dimension $(a+b)$. The data indicates that the average error in z_c is in general less than 25% of the average particle thickness ($\approx 2-3\mu m$) and the error grows as the observation distance increases. The average error in ϕ is about 2 to 4 degrees and the error show weak dependence on the observation distance L. Finally the average error in θ falls between 2 to 5 degrees, and the variation in the error increases with the observation distance L.

The dependence of z_c and θ error on the observation distance L arises from the nature of the reconstruction method and the PDMS gel. As the observation distance increases (Fr decreases into the far-field regime $Fr < 1$), the error in z_c and θ grows due to the limitation of the angular spectrum method, as well as the attenuation of the light through a thicker layer of PDMS gel. Figure 9 shows the image of the same particle reconstructed from the hologram at different observation distances. We find that the local PDMS gel structure introduces additional noise into the holograms that cannot be completely removed in the background subtraction process. This noise is present in all holograms and can affect the reconstruction quality.

We finally compare our reconstruction method to the method proposed by Byeon et al.[4],[5]. In their work, the holograms are propagated using the identical angular spectrum method to reconstruct the image at different z positions. For determining the particle center of mass in the z direction, the method assumes the particle to be a perfect spheroid and treats the particle as a convex lens. Once the position of the focal point (i.e., the location where the light beam crosses) and the focal length of the lens is known, one can extend from the focal point by the distance of focal length to find z_c of the particle. For a spheroidal lens with semi-minor axis length b, the focal length f of the lens can be calculated by the following eqn. (13)[5]:

$$f = \frac{n_{med}}{n_{lens} - n_{med}} \frac{b}{2}, \tag{13}$$

where n_{lens} and n_{med} represents the refractive index of the lens material and the surrounding medium, respectively. In our system, we have $n_{lens} = n_{PS} = 1.59$ and $n_{med} = n_{PDMS} = 1.42$. The ϕ angle of the particle can be determined by thresholding the image near the focal point and estimating the orientation of the bright stripe. As for determining the θ angle of the particle, however, the method proposed by Byeon et al.[5] relies on a rather ambiguously defined detection process, and a direct quantitative comparison will be difficult. We therefore only compare the detection result of z_c and ϕ between the two methods.

The detection error using the method by Byeon et al.[4],[5] is shown in figure 8a-b with blue color. In general, the method by Byeon et al.[4],[5] gives similar amount of error in z_c in comparison to the method proposed in this work. The error in z_c also similarly grows with increasing L due to the limited applicability of angular spectrum method in the near-field regime ($Fr \leq 1$). The method shows similar accuracy in detecting the ϕ angle compared to our method. We note that the method by Byeon et al.[4],[5] uses the exact particle dimensions for calculating the particle focal distance and the correct z_c location. In our work, we use the average major/minor axis length and aspect ratio acquired by bulk measurements to help us determine the process parameters and identify the proper detection region. This design can achieve comparable detection accuracy in z_c and ϕ as Byeon's method. Our method in addition provides a more clearly defined framework for identifying the particle's 3-D tilt angle θ.

4.5 Comparison to line fitting reconstruction methods

Line segment fitting methods are commonly used for detecting the 3-D orientation of slender particles ($A_R \gg 1$) such as metal nano-rods, malaria cells and E. coli cells[27,33,34,36,43]. For the

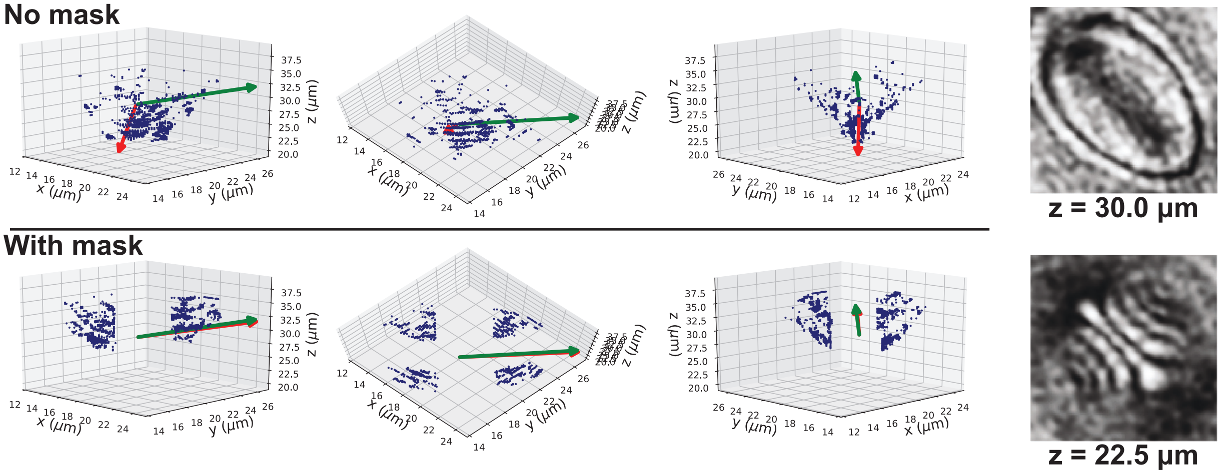

Fig. 10 Visualization of the line fitting results with and without a masking procedure. The extracted strong variance intensity pixels are shown as blue dots. The red arrow is the direction of the first principal component of the extracted pixels and the green arrow is the ground truth orientation from confocal microscopy ($\theta = 18.3°$). If no mask is applied, the lens effect shown in the $z = 22.5\ \mu m$ the picture distorts the pixel pattern so much that the orientation detection is incorrect ($\theta = 63.4°$). When mask is applied, the detected orientation is $\theta = 17.1°$. The particle center of mass for this particle is located at $z_c = 30\,\mu m$ and the sharp patterns from the lens effect appears around the focal point of the particle $z = 22.5\,\mu m$.

semi-transparent ellipsoidal particle with $O(1)$ aspect ratio used in this work, line fitting methods may not give reasonable detection results since the particle boundary pixels do not form a straight line. The patterns from the lens effect may also significantly affect the detection result. To elaborate this point, we examine holograms of an $A_R = 3$ prolate polystyrene particle taken at $L = 30\,\mu m$ as an example. We follow the procedures in section 3.2.2 to extract the gradient intensity profile around its center of mass at $z_c = 30\ \mu m$ and record the location of pixels where an abrupt change in pixel value is observed. We apply PCA to the recorded data without masking and extract the eigenvector of the first principal component as the direction of the best-fit line. The out-of-plane orientation of the best fit line is compared to the detected orientation by confocal microscopy. The top and bottom row of figure 10 shows the location of the particle boundary pixels when mask is not applied and applied, respectively. The green and red arrows in the figure show the particle orientation obtained from the confocal microscopy experiments and the first principal component of PCA, respectively. The confocal result gives $\theta = 18.3°$. When no mask is applied, the patterns from the lens effect significantly distort the detection results and yield an incorrect estimation of the particle orientation ($\theta = 63.4°$). When a mask is applied to cover the sharp patterns from the lens effect, the remaining pixels can better capture the location of the boundary pixels and gives a more accurate detection of the particle orientation ($\theta = 17.1°$).

4.6 Motion of an E. coli cell in aqueous medium

We finally demonstrate the ability of the method to analyze the 3-D motion of E. coli cells from a holographic video footage. The E. coli samples are prepared following the steps in section 2.2. The average major axis length is about 5 μm and the aspect ratio is 5. The holographic video is taken using the same experimental setup as described in section 2 at a rate of 24 fps, and the length of the footage is 14 seconds. Figure 11a shows a snapshot of the video footage. The full video footage can be found in the supplemental materials. We specifically reconstruct the position and orientation trajectories with respect to time for the four E. coli cells in the red boxes of figure 11a. Due to the opacity of the bacteria cells, we will not apply the center mask in the analysis ($W_m = 0$). To cope with the slender shape of the cells, we use $W_c = 0.6a$ and $N = 25$ for the reconstruction. Figure 11b shows the superimposed particle trajectory in the $x-y$ plane. The inset image shows one of the reconstructed frames. Figure 11c shows the 3-D visualization of each cell's position and orientation trajectory, where the dots and arrows represents the center of mass and orientation of the bacteria cell. The blue and red dots mark the location of the cell at the beginning and in the end of the footage, respectively.

The plots of the z_c, ϕ and θ trajectories of cell # 1 with respect to the video time is shown in figure 11d. The trajectories of the other 3 cells are available in supplementary material figures S1-S3. The E. coli cell migrates over a distance of 52 μm in the 14 second time interval, and the z_c of the cell fluctuates between 17 to 20 μm above the hologram plane. The orientation data shows that the cell first migrates along its major axis direction and gradually turns into a log-rolling motion with the θ angle seesawing around $\theta = 0$. Finally we note that the method is also able to capture the motion of a bacteria cell whose orientation is nearly perpendicular to the image plane (cell #4). The results in this section demonstrate the ability of the method to resolve the motion of a dynamic microparticle in 3-D space. The results also demonstrate that the method is applicable to both semi-transparent and opaque particles.

5 Conclusions

In this work, we developed a methodology that allows us to retrieve the 3-D information of a non-spherical microparticle via in-line digital holography. We applied the angular spectrum method to reconstruct an image at different z positions, and used the gradient intensity information to locate the out-of-plane particle center of mass z_c and the in-plane orientation ϕ. A principal component analysis is applied to the gradient intensity profiles to extract the out-of-plane θ angle of the particle. For semi-transparent particles with $O(1)$ aspect ratio, we utilized the image moment information to generate masks during the image sharpness evaluation process. The mask covers the diffraction patterns from the lens effect and helps us better locate the correct particle center of mass location. The process parameters such as W_c, W_m are tailored based on the average dimension of the particle. We verified the proposed method by comparing with confocal microscopy measurements. The detection error in z_c falls within 25% of the average particle thickness $(a+b)$, and the average errors in ϕ and θ are about 2° and 4°, respectively. The reconstruction error in general grows with longer observation distance L (smaller Fr) due to the limitation on the angular spectrum method as well as the attenuation of light signal through a thicker layer of PDMS gel. The reconstruction quality is also sensitive to the noise caused by the local PDMS structure. We also verified that our method shows similar detection accuracy in z_c and ϕ as the method proposed by Byeon *et al.*[4,5]. This method also provides a more clearly defined framework to identify the out-of-plane tilt angle. We finally demonstrated the ability of the method to process holographic video footage and quantitatively analyze the 3-D motion of opaque E. coli cells. This method provides a adequate accuracy in z_c for applications where errors on the order of particle size are acceptable – e.g., tracking micron size objects in macroscopic flows. To gain a better resolution in the depth direction, one can possibly utilize additional laser beams at a tilted angle to gain additional information in the depth direction[19,47]. For particles with similar length scale as the light wavelength, methods that tackle the reverse problem via hologram simulation and statistical inference[28,29,31] can provide better accuracy.

Conflicts of interest

The authors report no conflict of interest.

Acknowledgements

We thank Mr. Nick Humphrey for the help on design and fabrication of the film stretching device. Cheng-Wei Tai and Vivek Narsimhan acknowledge the financial support from American Chemical Society Petroleum Research Fund (ACS PRF 61266-DNI9). Arezoo M. Ardekani acknowledges NSF grant CBET-2141404.

Notes and references

1 E. K. Sackmann, A. L. Fulton and D. J. Beebe, Nature, 2014, **507**, 181–189.

2 F. Del Giudice, M. Tassieri, C. Oelschlaeger and A. Q. Shen, Macromolecules, 2017, **50**, 2951–2963.

3 N. Shokeen and A. Mukhopadhyay, Colloid and Polymer Science, 2021, **299**, 1595–1603.

4 H. Byeon, T. Go and S. J. Lee, Applied Optics, 2016, **54**, 2106–2112.

5 H. Byeon, T. Go and S. J. Lee, Optics Express, 2016, **24**, 598–610.

6 G. W. Graham and W. A. M. Nimmo Smith, Limnology and Oceanography: Methods, 2010, **8**, 1–15.

7 L. Yao, J. Chen, P. Sojka, X. Wu and K. Cen, Optics Letters, 2018, **43**, 1283.

8 L. A. Philips, D. B. Ruffner, F. C. Cheong, J. M. Blusewicz, P. Kasimbeg, B. Waisi, J. R. McCutcheon and D. G. Grier, Water Research, 2017, **122**, 431–439.

9 C. Schweizer, S. Prasad, A. Saini, C. V. Mashuga and W. D. Kulatilaka, Powder Technology, 2020, **376**, 612–621.

10 G. Li and A. M. Ardekani, Physical Review Letters, 2016, **117**, 1–5.

11 S. Bianchi, F. Saglimbeni and R. Di Leonardo, Physical Review X, 2017, **7**, 1–9.

12 A. Ahmadzadegan, S. Wang, P. P. Vlachos and A. M. Ardekani, Physical Review E, 2019, **100**, 62605.

13 R. V. More and A. M. Ardekani, Physical Review E, 2021, **103**, 1–13.

14 T. Garting and A. Stradner, Small, 2018, **14**, year.

15 Ó. Guadayol, T. Mendonca, Mariona Segura-Nogueraa Amand, J. Wright, M. Tassieri and S. Humphries, Proceedings of the National Academy of Sciences of the United States of America, 2020, **118**, year.

16 J. P. Binagia and E. S. Shaqfeh, Physical Review Fluids, 2021, **6**, 1–18.

17 D. R. Guildenbecher, M. A. Cooper, W. Gill, H. L. Stauffacher, M. S. Oliver and T. W. Grasser, Optics Letters, 2014, **39**, 5126.

18 K.-b. Im, S. Han, H. Park, D. Kim and B.-m. Kim, 2005, **13**, 5151–5156.

19 F. Saglimbeni, S. Bianchi, A. Lepore and R. Di Leonardo, Optics Express, 2014, **22**, 13710.

20 L. van der Graaff, G. J. L. H. van Leenders, F. Boyaval and S. Stallinga, Biomedical Optics Express, 2019, **10**, 6313.

21 D. Gabor, Nature, 1948, **161**, 777–778.

22 J. W. Goodman, Introduction to Fourier Optics, McGraw-Hill Companies, Inc., 4th edn, 2017.

23 J. Katz and J. Sheng, Annual Review of Fluid Mechanics, 2010, **42**, 531–555.

24 P. Memmolo, L. Miccio, M. Paturzo, G. D. Caprio, G. Coppola, P. A. Netti and P. Ferraro, Advances in Optics and Photonics, 2015, **7**, 713.

25 L. Lorenz, Det Kongelige Danske Videnskabernes Selskabs Skrifter, 1890, **6**, 1–62.

26 G. Mie, Annalen der Physik, 1908, **330**, 377–445.

27 F. C. Cheong, B. J. Krishnatreya and D. G. Grier, Optics Express, 2010, **18**, 13563.

28 T. G. Dimiduk and V. N. Manoharan, Optics Express, 2016, **24**, 24045.

29 M. A. Yurkin and A. G. Hoekstra, Journal of Quantitative Spectroscopy and Radiative Transfer, 2011, **112**, 2234–2247.

30 A. Wang, T. G. Dimiduk, J. Fung, S. Razavi, I. Kretzschmar, K. Chaudhary and V. N. Manoharan, Journal of Quantitative Spectroscopy and Radiative Transfer, 2014, **146**, 499–509.

31 R. Alexander, B. Leahy and V. N. Manoharan, Journal of Applied Physics, 2020, **128**, 060902.

32 Y. Wu, X. Wu, J. Yang, Z. Wang, X. Gao, B. Zhou, L. Chen, K. Qiu, G. Gérard and K. Cen, Applied Optics, 2014, **53**, 556.

33 M. Kempkes, E. Darakis, T. Khanam, A. Rajendran, V. Kariwala, M. Mazzotti, T. J. Naughton and A. K. Asundi, Optics Express, 2009, **17**, 2938.

34 F. C. Cheong and D. G. Grier, Optics Express, 2010, **18**, 6555.

35 T. Khanam, M. Nurur Rahman, A. Rajendran, V. Kariwala and A. K. Asundi, Chemical Engineering Science, 2011, **66**, 2699–2706.

36 L. G. Wilson, L. M. Carter and S. E. Reece, Proceedings of the National Academy of Sciences of the United States of America, 2013, **110**, 18769–18774.

37 F. C. Groen, I. T. Young and G. Ligthart, Cytometry, 1985, **6**, 81–91.

38 P. Langehanenberg, G. von Bally and B. Kemper, 3D Research, 2011, **2**, 1–11.

39 K. W. Seo, H. J. Byeon and S. J. Lee, Optics Letters, 2014, **39**, 3915.

40 C. Ho, A. Keller, J. A. Odell and R. Ottewill, Colloid Polym. Sci., 1993, **271**, 469–479.

41 J. A. Champion, Y. K. Katare and S. Mitragotri, Proceedings of the National Academy of Sciences of the United States of America, 2007, **104**, 11901–11904.

42 A. Ahmadzadegan, S. Wang, P. P. Vlachos and A. M. Ardekani, Phys. Rev. E, 2019, **100**, 062605.

43 M. Molaei, M. Barry, R. Stocker and J. Sheng, Phys. Rev. Lett., 2014, **113**, 068103.

44 M. R. Teague, Journal of the Optical Society of America, 1980, **70**, 920–930.

45 M. Pawlak and X. Liao, Proceedings - International Conference on Pattern Recognition, 1992, **3**, 549–552.

46 J. Gillespie and R. A. King, Pattern Recognition Letters, 1989, **9**, 19–25.

47 S. Bianchi, F. Saglimbeni, G. Frangipane, D. Dell'Arciprete and R. Di Leonardo, Soft Matter, 2019, **15**, 3397–3406.

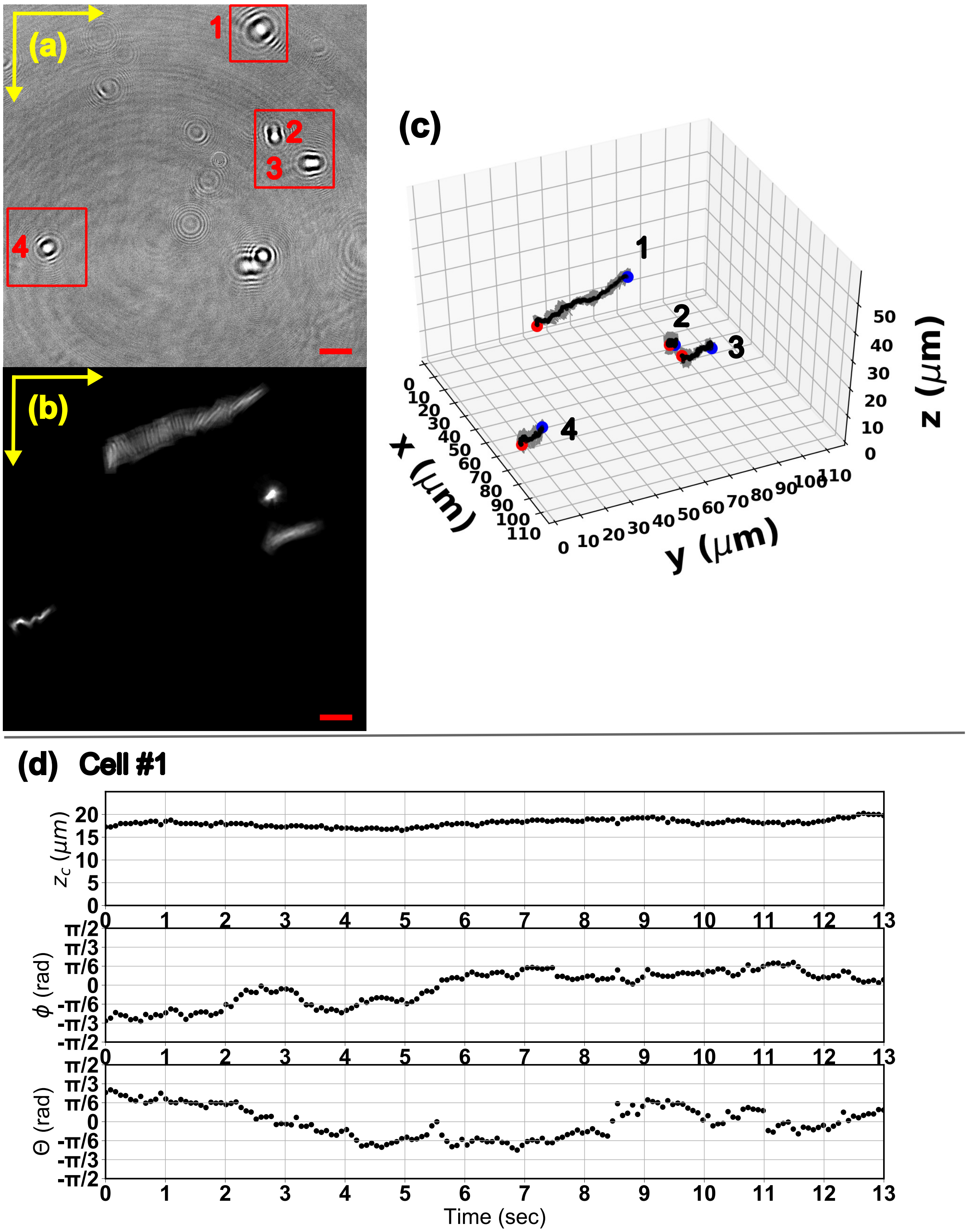

Fig. 11 (a) A snapshot of the holographic video footage of E. coli cell moving in a motility medium. We specifically follow the 4 bacterial cells in the red boxes. (b) The superimposed cell trajectories in the $x-y$ plane. (c) The 3-D visualization of the cell trajectories. The dots and arrows represent the cell center of mass and orientation. The blue and red dots mark the starting and ending location of the cell, respectively. (d) The z_c, θ and ϕ trajectory of cell # 1 with respect to the video time. The scale bar for all the figures is 10 μm. The video footage of all cells is found in the supplementary materials. The detailed trajectories for cells #2-4 can be found in supplementary materials figures S1-S3.